RESEARCH ARTICLE

Key Points:
- Comprehensive analyses of the excitation mechanism of fast magnetosonic waves observed by Van Allen Probes is performed
- Although substantial growth of half harmonic modes is predicted, the nonlinear evolution allowed the full harmonic modes to grow stronger
- The observed proton distribution corresponds to a marginally stable state as a result of interactions with the excited waves

Supporting Information:
- Supporting Information S1

Correspondence to:
K. Min,
kyungguk.min@jhuapl.edu

Fast Magnetosonic Waves Observed by Van Allen Probes: Testing Local Wave Excitation Mechanism

Kyungguk Min[1] (ID), **Kaijun Liu[2]** (ID), **Xueyi Wang[2]** (ID), **Lunjin Chen[3]** (ID), and **Richard E. Denton[4]** (ID)

[1]The Johns Hopkins University Applied Physics Laboratory, Laurel, MD, USA, [2]Department of Physics, Auburn University, Auburn, AL, USA, [3]Department of Physics, University of Texas at Dallas, Richardson, TX, USA, [4]Department of Physics and Astronomy, Dartmouth College, Hanover, NH, USA

Abstract Linear Vlasov theory and particle-in-cell (PIC) simulations for electromagnetic fluctuations in a homogeneous, magnetized, and collisionless plasma are used to investigate a fast magnetosonic wave event observed by the Van Allen Probes. The fluctuating magnetic field observed exhibits a series of spectral peaks at harmonics of the proton cyclotron frequency Ω_p and has a dominant compressional component, which can be classified as fast magnetosonic waves. Furthermore, the simultaneously observed proton phase space density exhibits positive slopes in the perpendicular velocity space, $\partial f_p/\partial v_\perp > 0$, which can be a source for these waves. Linear theory analyses and PIC simulations use plasma and field parameters measured in situ except that the modeled proton distribution is modified to have larger $\partial f_p/\partial v_\perp$ under the assumption that the observed distribution corresponds to a marginally stable state when the distribution has already been scattered by the excited waves. The results show that the positive slope is the source of the proton cyclotron harmonic waves at propagation quasi-perpendicular to the background magnetic field, and as a result of interactions with the excited waves the evolving proton distribution progresses approximately toward the observed distribution.

1. Introduction

First identified as equatorial noise (Russell et al., 1970), proton cyclotron harmonic waves are one of the frequently observed electromagnetic waves in the terrestrial magnetosphere. Early studies (Boardsen et al., 1992; Gulelmi et al., 1975; Laakso et al., 1990; Perraut et al., 1982) showed that the observed wave properties are consistent with those of the cold plasma fast magnetosonic mode. So the waves with proton cyclotron harmonic dispersion are widely referred to as fast magnetosonic waves (see Santolík et al., 2016, Introduction). In fact, the experimentally deduced dispersion relation has been shown to agree with that based on cold plasma theory (Boardsen et al., 2016; Walker & Moiseenko, 2013; Walker et al., 2015).

Observations show that fast magnetosonic waves are primarily confined to a narrow range of the geomagnetic equator (magnetic latitude less than 5°) (Boardsen et al., 1992, 2016; Hrbáčková et al., 2015; Meredith et al., 2008; Němec et al., 2005, 2006; Němec, Santolík, Hrbáčková, Cornilleau-Wehrlin, 2015; Posch et al., 2015; Russell et al., 1970; Santolík et al., 2002, 2004) and occur both inside and outside of the plasmapause at radial distances between 2 and 7 R_E (Gurnett, 1976; Laakso et al., 1990; Ma et al., 2013; Perraut et al., 1982). They can also occasionally occur at significantly larger radial distances (Hrbáčková et al., 2015) and latitudes (Tsurutani et al., 2014; Zhima et al., 2015). The polarization of the magnetic and electric field fluctuations, $|\delta B_\parallel| \gg |\delta B_\perp|$ and $|\delta E_\perp| \gg |\delta E_\parallel|$, indicate wave propagation very oblique/quasi-perpendicular to $\mathbf{B}_0$ (e.g., Curtis & Wu, 1979; Gary et al., 2010; Horne et al., 2000; Laakso et al., 1990; Liu et al., 2011), where $\mathbf{B}_0$ is the background magnetic field, $\delta\mathbf{B}$ and $\delta\mathbf{E}$ denote the magnetic and electric field fluctuations, and the directional subscripts denote directions with respect to $\mathbf{B}_0$. In many cases, these waves occur as a series of narrow tones spaced at multiples of the (equatorial) proton cyclotron frequency, Ω_p, up to the lower hybrid resonant frequency (e.g., Balikhin et al., 2015), but in other cases the harmonic spacing can differ from Ω_p determined at the observation point, or there can be no harmonic structure at all but an unstructured hiss-like spectrum (e.g., Posch et al., 2015). The general consensus is that the waves are generated at harmonics of Ω_p at the source region, but quasi-perpendicular propagation of the waves from potentially multiple source regions can lead to the other cases (e.g., Perraut et al., 1982; Su et al., 2017; Xiao et al., 2012; Zhima et al., 2015). Besides, radial and azimuthal propagation, combined with wave trapping by density gradients, may account for the origin of some of the

wave occurrence inside the plasmapause, which otherwise could not be explained by the local excitation mechanism (Ma, Li, Chen, Thorne, & Angelopoulos, 2014; Ma, Li, Chen, Thorne, Kletzing, et al., 2014). In addition, recent observations show a short-timescale (∼minute) quasi-periodicity of wave amplitude with a frequency-time dispersion (similar to chorus chirps) (Boardsen et al., 2014; Fu, Cao, et al., 2014; Li et al., 2017; Němec, Santolík, Hrbáčková, Pickett, & Cornilleau-Wehrlin, 2015; Walker et al., 2016), whose cause is still unclear. Fast magnetosonic waves can interact with the local radiation belt electron population resonantly and nonresonantly, efficiently accelerating some particles to high energies while scattering others into the loss cone (e.g., Albert et al., 2016; Artemyev et al., 2015; Bortnik et al., 2015; Chen et al., 2015; Horne et al., 2007; Li et al., 2014, 2015, 2016; Maldonado et al., 2016; Ma et al., 2016; Mourenas et al., 2013; Ni et al., 2017; Shprits, 2016; Shprits et al., 2013; Tao & Li, 2016; Yang et al., 2014; Xiao, Yang, et al., 2015).

Within the framework of linear Vlasov theory for electromagnetic fluctuations in a homogeneous, magnetized, and collisionless plasma, a series of proton cyclotron harmonic waves exist at propagation quasi-perpendicular to $\mathbf{B}_0$, satisfying $n\Omega_p < \omega_r < (n+1)\Omega_p$, where ω_r is the real frequency and n is an integer number. These waves, called ion Bernstein modes, can be unstable when the plasma consists of a ring-like proton velocity distribution which has a positive slope in the perpendicular velocity direction ($\partial f_p/\partial v_\perp > 0$) near $v_\parallel = 0$ (e.g., Curtis & Wu, 1979; Denton et al., 2010; Gary et al., 2010, 2011; Gulelmi et al., 1975; McClements et al., 1994; Perraut et al., 1982). Furthermore, for typical magnetospheric plasmas where cool background electrons and protons are dominant, these unstable modes at $\omega_r \approx n\Omega_p$ occur near those predicted from the cold plasma fast magnetosonic dispersion relation and exhibit properties consistent with the observed fast magnetosonic waves (e.g., Boardsen et al., 1992; Chen et al., 2010; Horne et al., 2000; Min & Liu, 2015b; Perraut et al., 1982). In this case, the ratio of the ring speed (nonzero perpendicular speed at which the ring-like proton distribution maximizes) to the Alfvén speed approximately determines the frequency range within which waves can be destabilized (Boardsen et al., 1992; Chen et al., 2010; Horne et al., 2000). There have been several studies suggesting or directly showing fast magnetosonic waves accompanied by a proton velocity distribution with $\partial f_p/\partial v_\perp > 0$ (Balikhin et al., 2015; Boardsen et al., 1992; Ma, Li, Chen, Thorne, & Angelopoulos, 2014; Meredith et al., 2008; Perraut et al., 1982; Xiao et al., 2013; Xiao, Zhou, et al., 2015; Zhou et al., 2014). And the linear Vlasov theory predicts wave growth patterns qualitatively consistent with the observed frequency spectrum (Balikhin et al., 2015; Boardsen et al., 1992; Ma, Li, Chen, Thorne, & Angelopoulos, 2014). Such proton distributions are often modeled with a loss cone distribution (Boardsen et al., 1992; Gary et al., 2011; Horne et al., 2000), ring velocity distribution (McClements et al., 1994; Perraut et al., 1982), or shell velocity distribution (Ashour-Abdalla et al., 2006; Freund & Wu, 1988; Janhunen et al., 2003). In the terrestrial magnetosphere, they are known to result from discrete nightside injections of plasma sheet ions during substorms or from the energy-dependent proton drift (Chen et al., 2010; Coroniti et al., 1972; Jordanova et al., 2012; Thomsen et al., 2011, 2017).

Relatively fewer kinetic simulations have been carried out to address the nonlinear consequences of the ion Bernstein instability. Janhunen et al. (2003) considered ion shell distributions and carried out two-dimensional electrostatic simulations to explain electron energization above auroral inverted-V regions. Ashour-Abdalla et al. (2006) examined ion Bernstein modes driven by ion shell distributions, which were shown from Cluster observations coincident with electrostatic emissions. Liu et al. (2011) performed the first electromagnetic simulations of the ion Bernstein instability. These authors also considered proton shell velocity distributions to exclude the temperature anisotropy-driven electromagnetic ion cyclotron (EMIC) instability. The two-dimensional particle-in-cell (PIC) simulation results agree well with the kinetic linear dispersion analysis of Denton et al. (2010) and Gary et al. (2010) and demonstrate that proton scattering by the enhanced fluctuations is a prime cause for the reduction of $\partial f_p/\partial v_\perp > 0$ and the consequent saturation of instability growth. Gao et al. (2017) considered the same shell proton distribution as in Liu et al. (2011) but used a gyrokinetic electron/full kinetic ion (GeFi) code (Lin et al., 2005, 2011) that allowed a larger proton-to-electron mass ratio. They showed that the mass ratio does not alter the essential properties of the excited waves although the number of harmonic modes increases with the mass ratio. Min and Liu (2016b) and Min et al. (2016) considered ring and anisotropic partial shell velocity distributions, which can drive both the ring-driven Bernstein instability and the temperature anisotropy-driven EMIC instability. The results show that although the maximum growth rate of the EMIC instability was consistently smaller than the theoretical growth rate of the fastest growing Bernstein mode, the PIC simulations consistently yielded larger saturation amplitudes for the EMIC instability even for a moderate temperature anisotropy. Sun et al. (2016) performed one-dimensional PIC simulations with a varying proton-to-electron mass ratio (m_p/m_e), light to Alfvén speed ratio (c/v_A), the ring
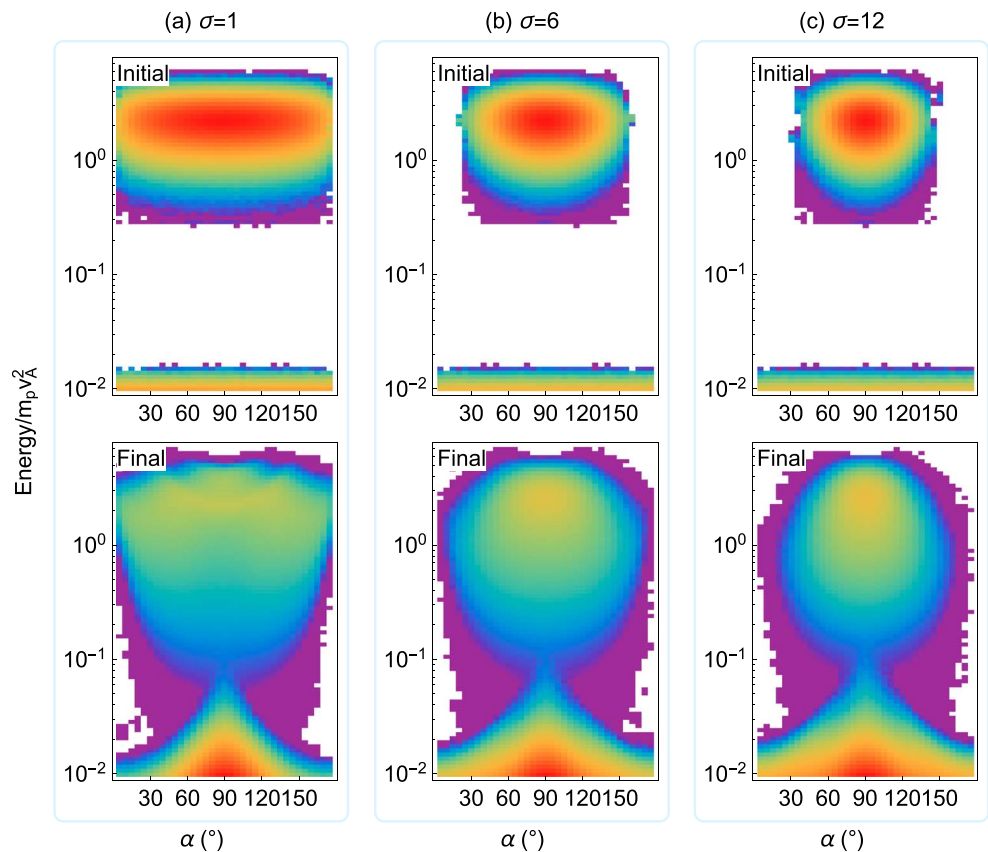
Figure 1. (top row) Initial and (bottom row) final (after fast magnetosonic wave saturation but well before EMIC wave saturation) proton differential fluxes (i.e., $j = p^2 f$; in log scale) as a function of energy and pitch angle from the PIC simulations of Min et al. (2016). Each column corresponds to a different level of initial pitch angle anisotropy indicated by the σ parameter labeled (see equation (1)). The white patches denote no simulation particles in that velocity space. The color scales are arbitrary in magnitude.

proton concentration (n_r) and the ring speed (v_r). At propagation perpendicular to $\mathbf{B}_0$, the increase of m_p/m_e, c/v_A, or n_r tends to result in a continuous spectrum of fast magnetosonic waves, and the increase of v_r leads to a discrete spectrum covering broader frequency space. These results are consistent with the linear theory prediction of Chen et al. (2016). Sun et al. (2017) used the same simulation model for varying wave normal angles adjacent to perpendicular directions and showed that the parallel electric field fluctuations can efficiently energize the background electrons in directions parallel to $\mathbf{B}_0$.

The motivation of the present study is to use the lessons learned from earlier simulation studies to interpret fast magnetosonic wave observations, particularly those locally excited. The following two points may be important to consider for such a study. First, as expected from quasilinear theory (Horne et al., 2000; Laakso et al., 1990), interactions with fast magnetosonic waves result in the scattering of energetic ring and cool background protons predominantly in the perpendicular velocity direction (see, e.g., Min & Liu, 2016b, Figures 4 and 8). Figure 1 displays snapshots of the initial and final (defined to be some time after the fast magnetosonic wave saturation but well before the EMIC wave saturation) proton differential fluxes as a function of energy and pitch angle taken from the PIC simulations in Min et al. (2016). The three cases presented were initialized with different levels of pitch angle anisotropy indicated by the σ parameter (see equation (1)). The energetic protons primarily diffuse to lose energy, and the energy lost is partially transferred to the heating of background protons that were initially isotropic. The presence of this feature in particle data can serve as evidence for concomitant fast magnetosonic waves being locally generated by energetic ring protons. At the same time, such a feature seen from the particle data indicates that the observed proton distribution is likely to be marginally stable to the ion Bernstein instability. This brings us to the second point. The linear growth rate obtained from the already evolved proton distribution may be substantially different from the observed wave spectrum. In quasilinear theory, the slowly varying wave amplitude results from time integration of the

instantaneous growth rate (Davidson & Ogden, 1975). For example, as shown in Tao et al. (2017, Figure 1) for a whistler anisotropy instability, the final wave spectrum can be different from that predicted by the instantaneous instability growth shortly after wave saturation. Therefore, direct comparison of an observed wave spectrum with the growth rate calculated from a particle distribution measured at a particular time can be misleading if the measurement is made after wave saturation.

In the present study, we analyze one event of fast magnetosonic waves and energetic protons measured by the Van Allen Probes (Mauk et al., 2013), and interpret them using the linear theory and kinetic simulations for electromagnetic fluctuations in a homogeneous, collisionless, magnetized plasma. We are concerned with wave excitation from a localized source near the magnetic equator where these assumptions may be applied. For simplicity, we assume that the waves are driven by an initial injection of energetic protons. Thus, kinetic simulations are initialized with an unstable proton distribution so that the waves can grow to a sufficiently large amplitude at saturation. An alternative, perhaps more realistic, approach may be continuously refreshing the distribution with fresh energetic protons, thereby mimicking continuous injections (Denton et al., 1993); such a model will not be considered here.

The paper is organized as follows. Section 2 describes the wave and particle observations, and section 3 presents the results for the simulations and compares them with the observations. Section 4 summarizes the results and discusses the model-observation comparison.

2. Observation

The Van Allen Probes (RBSP-A) detected fast magnetosonic wave activity on 7 April 2013 near the midnight sector. No geomagnetic storm was present prior to the event (the *Dst* index remained above -20 nT for at most 3 days prior to the event), but the *AE* index suddenly increased to 480 nT at about 1400 UT and stayed at 50 nT after 1520 UT for the rest of the day (not shown). Figures 2a and 2b show survey mode measurements from the Electric and Magnetic Field Instrument and Integrated Science (EMFISIS) instrumentation suite (Kletzing et al., 2013) of the magnetic field wave power, $|\delta B_U|^2 + |\delta B_V|^2 + |\delta B_W|^2$, and the electric field wave power without the spin component, $|\delta E_U|^2 + |\delta E_V|^2$, respectively. (The subscripts denote the spacecraft coordinate system where the W direction is along the spin axis.) The spin component of the electric field was excluded because of contamination from solar panel shadows during this time period. Relatively strong wave power appears roughly between 2115 and 2215 UT near the magnetic equator with an L shell $\lesssim 6$. At the same time, weak wave activity is present at least for the entire period shown. Figures 2c and 2d show omnidirectional proton differential fluxes from the Radiation Belt Storm Probes Ion Composition Experiment (RBSPICE) (Mitchell et al., 2013) and the Helium, Oxygen, Proton, and Electron (HOPE) Mass Spectrometer (Funsten et al., 2013) of the Energetic Particle, Composition, and Thermal Plasma (ECT) suite (Spence et al., 2013), respectively. In Figure 2e, the total electron density, n_e, was derived manually from the upper hybrid resonance line. Using n_e and the local magnetic field measurement, the Alfvén energy $m_p v_A^2/2$ was determined and superimposed in Figure 2d, where $v_A = B_0/\sqrt{4\pi m_p n_0}$ is the Alfvén speed, m_p is the proton mass, and n_0 is the total proton/plasma number density. The two local maxima of the proton flux above $m_p v_A^2/2$ can be a potential source for the concomitant fast magnetosonic waves.

During burst mode operation, the EMFISIS instrument samples the electric and magnetic fields at a rate of 35,000 samples/s for about 6 s. Fortuitously, during the time interval marked by the red bars in Figures 2a and 2b, the EMFISIS instrument was operating in burst mode almost continuously for about 20 min, meaning that 200 sets of these burst mode waveforms were captured without any temporal gaps. The individual 6 s long magnetic field fluctuations are Fourier transformed for presentation. Although not critical to the present study, calibrations are applied to the Fourier transformed results (see https://emfisis.physics.uiowa.edu/Waveform_Calibration). Because the proton cyclotron frequency is $f_{cp} \approx 2$ Hz, the frequency resolution $\Delta f = 1/6 \approx 0.167$ Hz is small enough to resolve the harmonic structure, if at all, of the fast magnetosonic waves. Figure 3a shows the magnetic field wave power as a function of time (vertical axis) and frequency normalized to f_{cp} (horizontal axis). (Each row of pixels corresponds to the Fourier transform of one set of 6 s long waveforms.) The harmonic structure of the frequency spectrum is evident between $8f_{cp}$ and $34f_{cp}$ with an isolated harmonic near $4f_{cp}$. The time average of the magnetic field wave power is shown in Figure 3b. Here the red and black curves correspond to the compressional ($|\delta B_\parallel|^2$) and transverse ($|\delta B_\perp|^2$) components, respectively. The harmonic pattern of the spectrum, the frequency range of the enhanced power, and $|\delta B_\parallel|^2 \gg |\delta B_\perp|^2$ indicate that these waves can be classified as fast magnetosonic waves (e.g., Boardsen et al., 2016). Moreover, the fact that a series
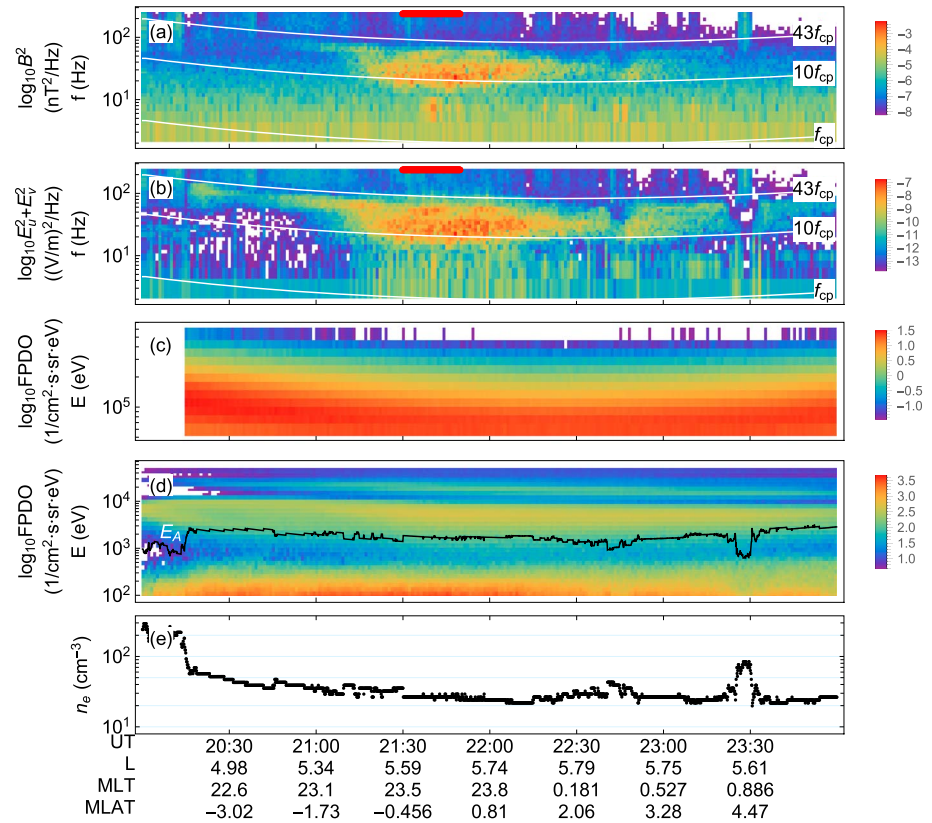
Figure 2. Summary plots of Van Allen Probe A measurements of the event on 7 April 2013. (a) EMFISIS survey mode total magnetic field power spectrum (i.e., $|\delta B_U|^2 + |\delta B_V|^2 + |\delta B_W|^2$, where the spacecraft spin direction is along the W direction and the U and V directions are perpendicular to each other and to the W direction). (b) EMFISIS survey mode partial electric field power spectrum without the spin component (i.e., $|\delta E_U|^2 + |\delta E_V|^2$). The three white curves in Figures 2a and 2b denote f_{cp} (the local proton cyclotron frequency), $10f_{cp}$ and $43f_{cp}$, respectively, and the red bars between 2130 and 2150 UT denote the period of burst mode operations. (c and d) Omnidirectional proton differential fluxes measured by the RBSPICE and HOPE instruments, respectively. The black curve in Figure 2d traces Alfvén energy $E_A \equiv m_p v_A^2/2$, where $v_A = B_0/\sqrt{4\pi n_e m_p}$ is the Alfvén speed calculated using the local parameters. (e) Total electron number density estimated from the upper hybrid frequency line.

of spectral peaks occur at exact integer multiples of f_{cp} suggests that these waves were locally generated (e.g., Balikhin et al., 2015).

Figure 4a shows the proton differential flux as a function of energy and pitch angle averaged for the first half (∼9 min) of the whole burst mode period (the flux for the second half is almost identical). It suggests that there are at least three populations: (1) the anisotropic population below 1 keV, (2) the population between 1 keV and 10 keV, and (3) the population within very small energy range near 20 keV. Figure 5 confirms that the intensities of the last two energetic populations are large enough to form two local maxima in the phase space density. The phase space density is monotonically decreasing above 50 keV. Therefore, either the second or the third populations which have positive slopes, or both, have the potential to excite the observed fast magnetosonic waves. The lower- and higher-energy parts delineated by the vertical dashed lines at about 50 keV correspond to the measurements from the HOPE and RBSPICE instruments, respectively. Because of mismatch between the two measurements, a factor of 3 is multiplied to the HOPE measurement so that the high-energy part of the HOPE measurement can be connected to the low-energy part of the RBSPICE measurement (see Min et al., 2017; Kistler et al., 2016). Unless otherwise specified, this adjustment is applied to the numerical analyses throughout. Section 4 discusses how the results can be affected if a smaller factor is applied.

Concentrations of heavier ion species measured by the HOPE instrument (between 30 eV and 54 keV) were at a very low level relative to the total electron density (less than 1%). Similarly, the electron number density above 30 eV measured by the HOPE instrument was below 1%, suggesting that the dominant electron population
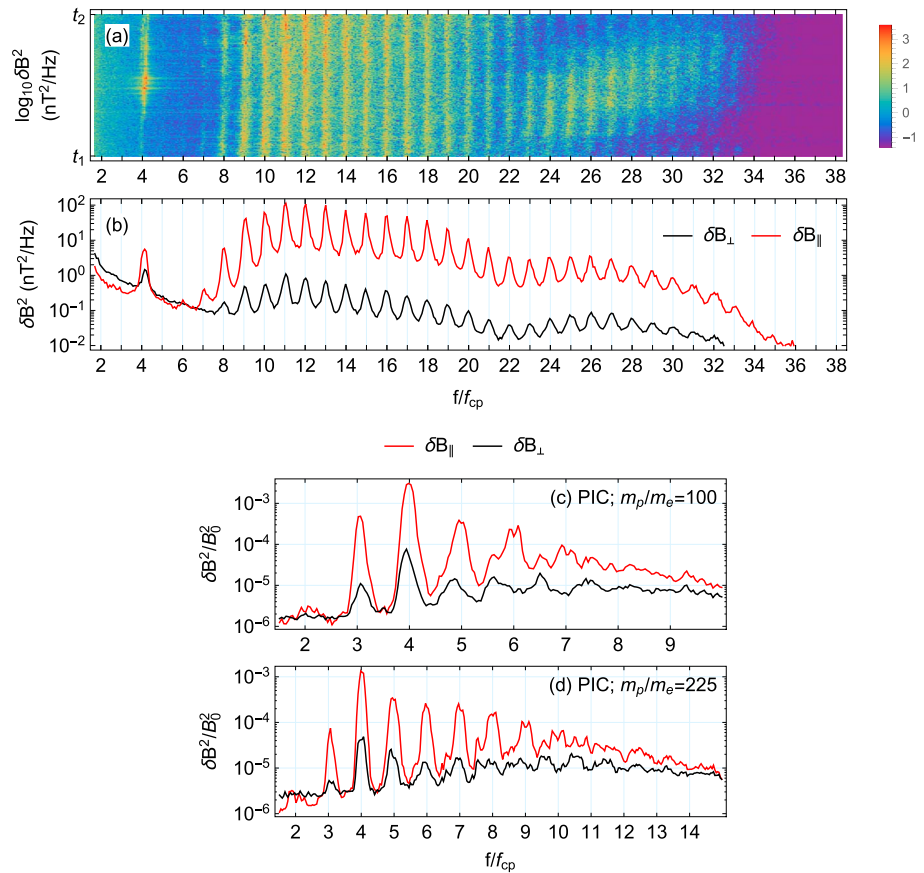
Figure 3. Magnetic field frequency power spectrum from the EMFISIS burst mode waveforms. (a) $|\delta\mathbf{B}|^2 = |\delta B_U|^2 + |\delta B_V|^2 + |\delta B_W|^2$ as a function of time (vertical axis) and frequency normalized to the local proton cyclotron frequency (bottom axis). The time t_1 and t_2 denote 2130 and 2150 UT, respectively. (b) Log averages of the compressional (red) and transverse (black) components of the frequency power spectrum. (c and d) Frequency power spectra of the magnetic field fluctuations from the PIC simulations with $m_p/m_e = 100$ and 225, respectively, in the same format as Figure 3b. Note that the absolute units are different between the observation and the simulations, but the relative scales are the same.
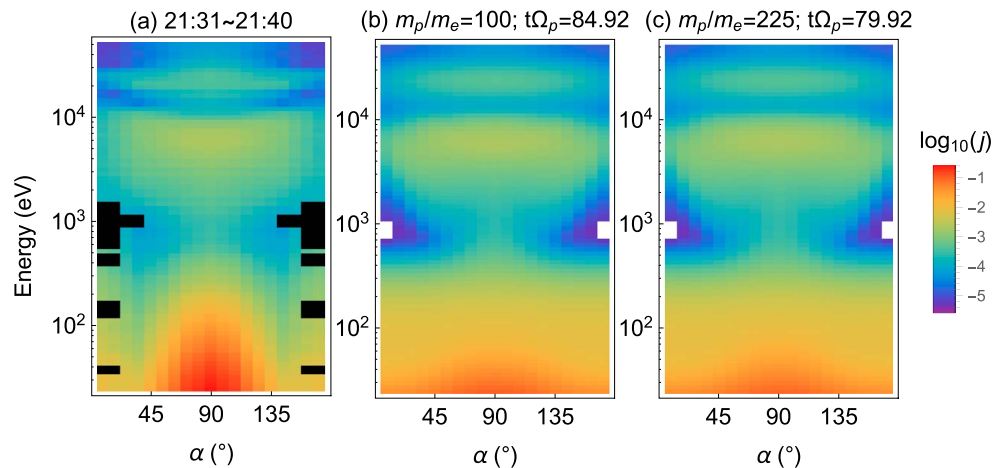

Figure 4. Proton differential fluxes from the observation and the simulations. (a) The time average of the fluxes measured between 2131 and 2140 UT (with a cadence less than half a minute) by the HOPE instrument as a function of energy and pitch angle. The right half is a mirror reflection of the left half assuming symmetry about $\alpha = 90°$. (b and c) The fluxes at wave saturation from the simulations with $m_p/m_e = 100$ and 225, respectively. All fluxes are normalized to have the same unit as the observations in Figure 4a. The black and white patches indicate invalid values and the values less than the lowest limit in the color scale, respectively.
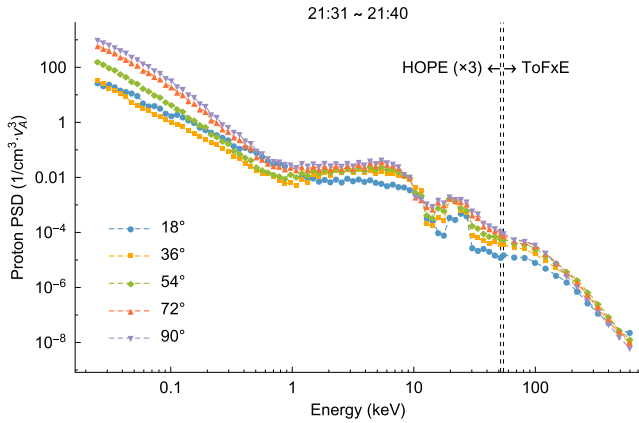
Figure 5. Proton phase space density as a function of energy at five pitch angle bins as labeled. The HOPE and RBSPICE (time of flight by energy product) measurements between 2131 and 2140 UT were taken into account. The vertical dashed lines delineate the measurements from the two instruments. A factor of 3 is multiplied to the HOPE measurement (see text).

was cool background electrons. Hence, we will consider a proton-electron plasma with a single electron population of low temperature for the analyses in the following section.

3. Simulations

In this section, PIC simulations are carried out using parameters consistent with the observation, and the resulting wave and proton distributions are compared with those observed. There are two difficulties with kinetic simulations. The first is determining the initial proton velocity distribution. Ideally, one would want to directly use the measured particle distribution to initialize the simulations. However, not only is this not practical because of the measurement quality (missing values, smoothness, limited energy coverage, etc.), but more fundamentally the comparison between Figures 1 and 4a suggests that the observed proton distribution might have already exhausted free energy through the wave excitation and subsequent heating of the thermal population. Because of this, Fu, Cowee, et al. (2014) chose to start their simulation of whistler waves with initial electron temperature anisotropies increased to excite the whistler waves. The same approach is adopted here; Figure 1 can provide guidance for choosing the initial conditions.

The second difficulty is carrying out full-scale simulations with the real proton-to-electron mass ratio of $m_p/m_e = 1{,}836$. Due to the increasing number of harmonic modes and the increasing extent of unstable wave number space with m_p/m_e (e.g., Min & Liu, 2016a), the simulation box size and the grid size should be respectively large and small enough to resolve both the shortest and longest wavelength modes. This cannot be done with limited computational resources available, so some compromise has to be made. We use a small value of m_p/m_e, while other parameters are kept the same as the observed values. The PIC code used for the present simulations was developed by Liu (2007) and applied to the ion Bernstein instability in Liu et al. (2011), Min and Liu (2016b), and Min et al. (2016). We perform two PIC simulations with $m_p/m_e = 100$ and 225, respectively. The effects of m_p/m_e on the ion Bernstein instability have been examined using linear theory (Min & Liu, 2016a) and simulations (Gao et al., 2017).

3.1. Initial Proton Distribution

Two analytic distribution functions are used as bases to represent the observed proton phase space density. The first is the partial shell distribution

$$f_j = \frac{n_j}{\pi^{3/2}\theta_j^3 C(v_j/\theta_j)} e^{-(v-v_j)^2/\theta_j^2} \sin^{\sigma_j}\alpha, \tag{1}$$

where n_j is the number density; α is the pitch angle; $v = \sqrt{v_\parallel^2 + v_\perp^2}$ with $v_\parallel$ and $v_\perp$ being parallel and perpendicular speeds, respectively; v_j is the shell speed; θ_j is the thermal spread of the shell; σ_j represents the degree of pitch angle anisotropy; the subscript j labels the population; and the constant denominator is

$$C(x) = \left[xe^{-x^2} + \sqrt{\pi}\left(0.5 + x^2 \mathrm{erfc}(-x)\right)\right] \frac{\Gamma(1+\sigma_j/2)}{\Gamma(1.5+\sigma_j/2)}. \tag{2}$$

Here $\mathrm{erfc}(x)$ is the complementary error function and $\Gamma(x)$ is the gamma function. Note that the initial energetic proton distributions of Figure 1 were initialized with this partial shell. Because this function maximizes at $v_\parallel = 0$ and $v_\perp = v_j$ for $\sigma_j > 0$, it can represent the two energetic proton populations with positive slopes in the observed phase space density (Figure 5). The second is the bi-Maxwellian distribution

$$f_j = \frac{n_j}{\pi^{3/2}\theta_{\parallel j}\theta_{\perp j}^2} e^{-v_\parallel^2/\theta_{\parallel j}^2} e^{-v_\perp^2/\theta_{\perp j}^2}, \tag{3}$$

where $\theta_{\parallel j} = \sqrt{2T_{\parallel j}/m_p}$ and $\theta_{\perp j} = \sqrt{2T_{\perp j}/m_p}$ are the parallel and perpendicular thermal speeds, respectively. Here $T_{\parallel j}$ and $T_{\perp j}$ are temperatures, respectively, parallel and perpendicular to $\mathbf{B}_0$. Equations (1) and (3) are normalized such that $\int d\mathbf{v} f_j = n_j$.

Table 1
Parameters for Model Proton Velocity Distributions

#	Model 1			Model 2		
	Bi-Maxwellian					
	n_j/n_e	$\theta_{\parallel j}/v_A$	$\theta_{\perp j}/v_A$	n_j/n_e	$\theta_{\parallel j}/v_A$	$\theta_{\perp j}/v_A$
1	0.376	0.0635	0.110	0.376	0.060	0.060
2	0.0526	0.192	0.210	0.0526	0.190	0.190
3	0.0104	0.759	1.25	0	×	×
4	0.00564	3.182	4.50	0.00564	3.182	4.50
	Partial shell[a]					
	n_j/n_e	θ_j/v_A	v_j/v_A	n_j/n_e	θ_j/v_A	v_j/v_A
5	0.0274	0.430	1.70	0.0378	0.430	1.70
6	0.00852	0.600	3.55	0.00852	0.600	3.55

[a]For the partial shell components, $\sigma_5 = \sigma_6 = 1$.

We use a combination of two partial shells and four bi-Maxwellians to represent the observed phase space density, in order to achieve a balance between quality of the model distribution and ease of numerical experiments. Table 1 (second to fourth columns) lists the fitting parameters for the six-component model, hereinafter labeled "Model 1." The fitting was done manually by minimizing the visual difference between the model and the observed phase space density through the following two steps. First, the parameters relevant to the phase space density at $\alpha = 90°$ (e.g., $\theta_{\perp j}$, and v_j) were determined. Second, the remaining parameters were adjusted to minimize the visual differences at lower pitch angles. Figure 6a shows the differential flux constructed from Model 1, and Figure 6c shows the model phase space density at $\alpha = 90°$ (red curve) in comparison with the observed phase space density (dots). The agreement at $\alpha = 90°$ is good as intended. However, there are some visual differences at off-90° pitch angles (especially the pitch angle anisotropy of the low-energy population, comparing Figures 4a and 6a). The discrepancy in the low-energy population is due primarily to the limitation of the assumed bi-Maxwellian—the observed distribution exhibits an enhanced field-aligned population, resulting in a nonmonotonic pitch angle profile. Nevertheless, the comparison with Figure 4a indicates that Model 1 represents the three population structures mentioned in the previous section.

For the reasons mentioned earlier in this section, we suppose that the measured proton distribution (similar to Model 1) has already exhausted free energy to excite the concomitant fast magnetosonic waves. Therefore, we have to somehow construct an initial proton distribution that will excite the observed fast magnetosonic waves and evolve into the observed distribution after wave saturation. With the guidance of Figure 1, we may be able to roll back some of the features in Model 1 that might have been caused by the wave excitation.
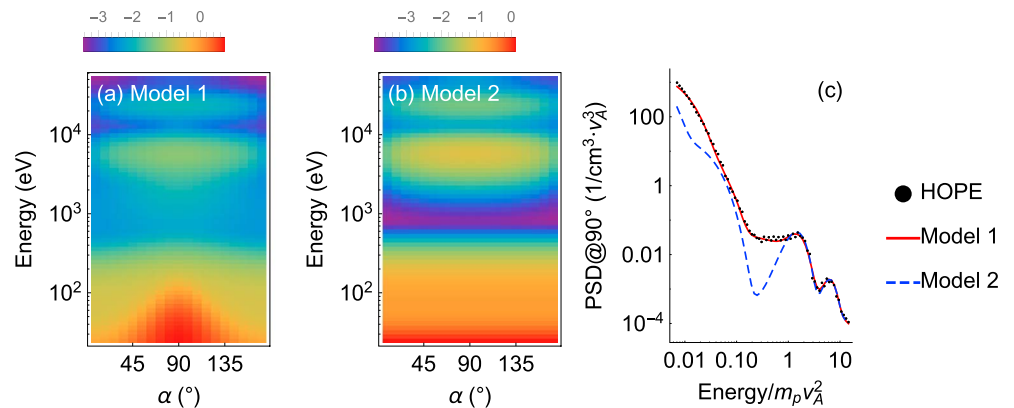

Figure 6. (a and b) Differential fluxes constructed from Models 1 and 2, respectively. The differential fluxes have arbitrary units. (c) Comparison of the phase space densities (PSD) at $\alpha = 90°$ between the observed PSD and the model representations. The dots, red solid curve, and blue dashed curve respectively denote the observation, Model 1, and Model 2. A factor of 3 is multiplied to the HOPE measurement (see text).

Two such features are of course the perpendicular heating of the thermal component and the perpendicular scattering of the partial shell component near 5 keV. Accordingly, we make two modifications to Model 1. First, the perpendicular temperatures of the two anisotropic thermal components (components 1 and 2 in Table 1) are reduced to make them isotropic, thus rolling back the perpendicular heating of the thermal protons. The second modification is to roll back the scattering of the partial shell component 5 in Table 1. Close examination suggests that the bi-Maxwellian component 3, which constitutes the proton population at ~2 keV (or $0.4m_p v_A^2$), can be considered as being scattered from the partial shell population. So we simply merge this component to the partial shell component 5. We do not change the σ parameters because Figure 1 indicates that the pitch angle anisotropy of the energetic ring/shell protons remains essentially unchanged. The parameters for this new model, labeled "Model 2," are listed in Table 1 (fifth to seventh columns). The corresponding differential flux and the phase space density at $\alpha = 90°$ are shown in Figures 6b and 6c, respectively, for comparison.

Additionally, the electron population is represented by a single Maxwellian with $\beta_e = 0.01$ where β_e is the ratio of the electron plasma pressure to the magnetic pressure, and the charge-neutralizing cool background proton population is represented by a Maxwellian with $\theta_c^2/v_A^2 = 0.001$. For the observed event, the electron plasma-to-cyclotron frequency is $\omega_{pe}/\Omega_{ce} \approx 12$.

3.2. Linear Theory

The two model distributions are used to solve the dispersion relation for electromagnetic fluctuations following the method of Min et al. (2016) (see also Appendix A). The calculations were done with $m_p/m_e = 1,836$. Figures 7a and 7b show linear growth rates (only growing modes, $\gamma > 0$) as a function of the parallel and perpendicular wave numbers. By comparing the maximum growth rates in the color bars (roughly a factor of 3 difference), Model 2 is more unstable to the Bernstein instability, which extends beyond the $k_\parallel$ axis limit of the figure (see, e.g., Min & Liu, 2016a, Figure 1). Fastest instability growth occurs at $k_\parallel c/\omega_{pp} = 0.5$ and $k_\perp c/\omega_{pp} = 34.8$ with complex frequency $\omega/\Omega_p = 28.5 + 0.0533i$ for Model 1, and at $k_\parallel c/\omega_{pp} = 0.05$ and $k_\perp c/\omega_{pp} = 29.9$ with $\omega/\Omega_p = 24.0 + 0.164i$ for Model 2. Here $\omega_{pp} = \sqrt{4\pi n_0 e^2/m_p}$ is the proton plasma frequency. In Figure 7c, the growth rates at $k_\parallel c/\omega_{pp} = 0.05$ are shown for the two models. For both cases, the growth rates maximize near integer multiples of Ω_p (full harmonics). Overall, the growth rate for Model 1 is smaller by almost an order of magnitude than that of Model 2. In addition, Figure 7a shows that the growth rates for Model 1 approach 0 as $k_\parallel \rightarrow 0$. This can be understood from the small positive slope of Model 1 near $v_\parallel = 0$ (e.g., Chen, 2015). In contrast, Model 2 maintains large growth rates even at $k_\parallel = 0$ because of the larger positive slope. With increasing $k_\parallel$, the growth rates decrease and reach the local minimum at $k_\parallel c/\omega_{pp} \approx 0.4$ (see Figures 7a and 7b). With a further increase of $k_\parallel$, the growth rates are enhanced again and reach the local maximum at $k_\parallel c/\omega_{pp} \approx 0.6$. Figure 7d shows the growth rates as a function of real frequency at $k_\parallel c/\omega_{pp} = 0.6$. The growth rate peaks now appear near half-integer multiples of Ω_p (half harmonics) for both cases. For even larger $k_\parallel$, growth rates at full harmonics are enhanced again (not shown). Min and Liu (2016a, 2016c) showed that the alternation between the full and half harmonics is an intrinsic property of the shell velocity distribution-driven ion Bernstein instability and is independent of m_p/m_e. For a given wave with a specific real frequency (ω_r) and parallel wave number ($k_\parallel$), particles at different parallel resonant speeds, $v_{\parallel res} \equiv (\omega_r - n\Omega_p)/k_\parallel$, most effectively interact with the wave and contribute to net wave growth/damping, where n is the cyclotron resonance order. For an isotropic shell ($\sigma = 0$) distribution, strong wave growth tends to occur when there are more n that result in $|v_{\parallel res}| \approx 0$ where the positive slope $\partial f_p/\partial v_\perp > 0$ maximizes and when there are fewer n that result in $|v_{\parallel res}| \approx v_s$ where the slope $\partial f_p/\partial v_\perp$ is largely negative. The (local) maxima of net growth/damping tend to alternatively occur when $2\omega_r/\Omega_p$ is integer and at every $\Delta k_\parallel = \Omega_p/(2v_s)$ (see Min & Liu, 2016c, Figures 5–7, and the related discussion). For proton component 5 whose shell speed is $1.7v_A$ and which contributes most to wave growth, $\Delta k_\parallel c/\omega_{pp} \approx 0.3$. So the first local minimum in $k_\parallel$ space is expected at $k_\parallel c/\omega_{pp} = 1.5\Delta k_\parallel c/\omega_{pp} \approx 0.44$. This is roughly consistent with the linear theory results in Figures 7a and 7b.

We may want to compare the linear theory results with the observations as previous studies have done. The primary focus of this comparison concerns instability growth at full versus half harmonics. Although Model 1 can excite full harmonic modes as the observations show, their growth rates are smaller than those of half harmonic modes (see Figures 7c and 7d). So as far as linear growth is concerned, the expectation is that the observations should have been swamped by the half harmonic modes. In contrast, Model 2 is capable of exciting strongest waves at full harmonics. This is more consistent with the observations and favors the hypothesis that the observed proton distribution corresponds to the marginally stable state when the distribution has
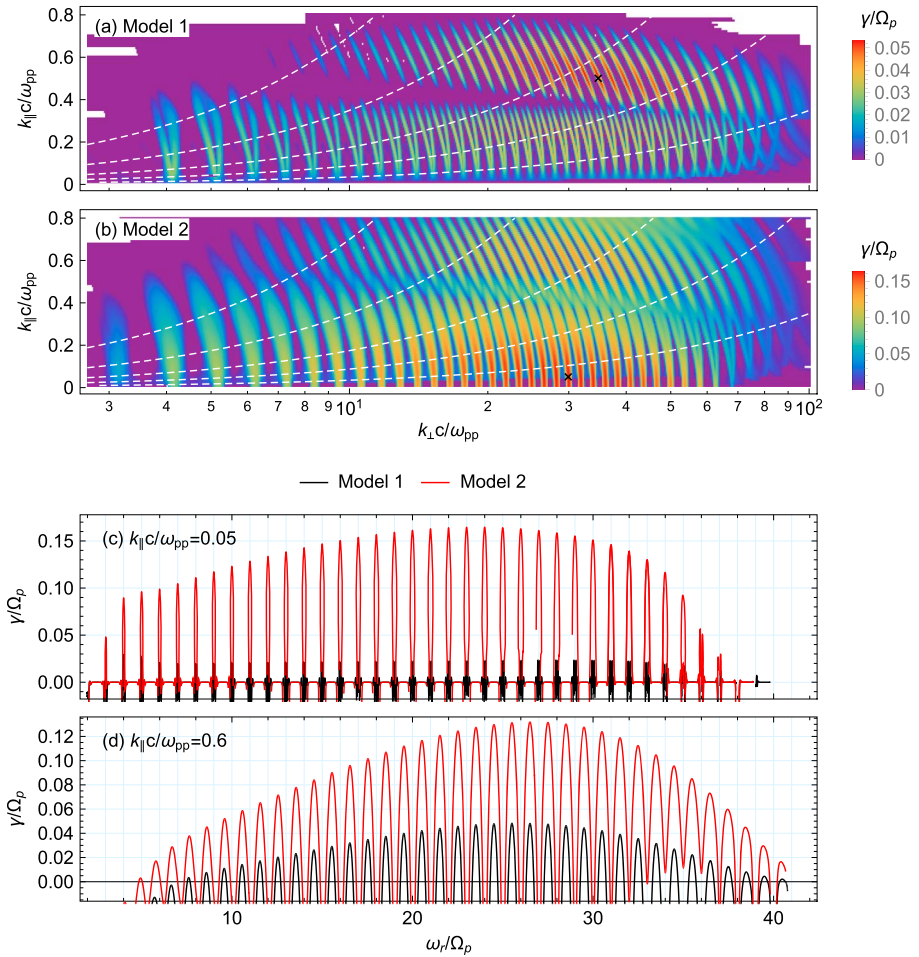
Figure 7. Linear growth rates of the ion Bernstein instability as a function of parallel and perpendicular wave numbers normalized to the ion inertial length, c/ω_{pp}, for (a) Model 1 and (b) Model 2. The cross symbols locate the fastest linear growth: $k_\parallel c/\omega_{pp} = 0.5$, $k_\perp c/\omega_{pp} = 34.8$ and $\omega/\Omega_p = 28.5 + 0.0533i$ for Model 1; $k_\parallel c/\omega_{pp} = 0.05$, $k_\perp c/\omega_{pp} = 29.9$ and $\omega/\Omega_p = 24.0 + 0.1643i$ for Model 2. The white dashed curves denote constant wave normal angle contours (from top to bottom, 86°, 88°, 89°, 89.5°, and 89.8°, respectively). Deep purple color denotes $\gamma/\Omega_p \leq 0$, and white patches are the region not covered or where no solutions were found. Comparison of the growth rates between the two model distributions (as labeled) at (c) $k_\parallel c/\omega_{pp} = 0.05$ and (d) $k_\parallel c/\omega_{pp} = 0.6$.

already been scattered by the excited waves. At the same time, Model 2 also predicts half harmonic modes that might be expected to be visible in the frequency spectrum because of their appreciable growth rates. In contrast, the observations in Figures 3a and 3b do not suggest that these half harmonic modes exist. Because the full harmonic modes would grow strongest, perhaps these half harmonic modes have much smaller amplitude than the full harmonic modes following nonlinear wave development. This possibility will be examined in the following PIC simulations.

3.3. PIC Simulation Results

PIC simulations are initialized with Model 2 in a two-dimensional rectangular box in the *x-y* plane. The background magnetic field $\mathbf{B}_0$ is in the *x* direction. The cell sizes are $\Delta\{x, y\} = \{0.15, 0.04\}c/\omega_{pp}$, and the number of cells $N_{\{x,y\}} = \{1,000, 1,000\}$. A periodic boundary condition is used in both dimensions. We use the light-to-Alfvén speed ratio $c/v_A = 120$. This means $\omega_{pe}/\Omega_{ce} = 12$ for the simulation with $m_p/m_e = 100$, but $\omega_{pe}/\Omega_{ce} = 8$ for the simulation with $m_p/m_e = 225$. The change of the lower hybrid frequency due to the slight decrease of ω_{pe}/Ω_{ce} for the simulation with $m_p/m_e = 225$ is less than 1%. In this way, we can use the same time step $\Delta t\Omega_{cp} = 0.000333$ for both simulations. A total of 7×10^8 simulation particles are used to represent the proton distribution (100 particles per cell and component). The cool background electron and proton populations are assumed to be Maxwellians with $\beta_e = 0.01$ and $\theta_c^2/v_A^2 = 0.001$, respectively. The simulation runs were
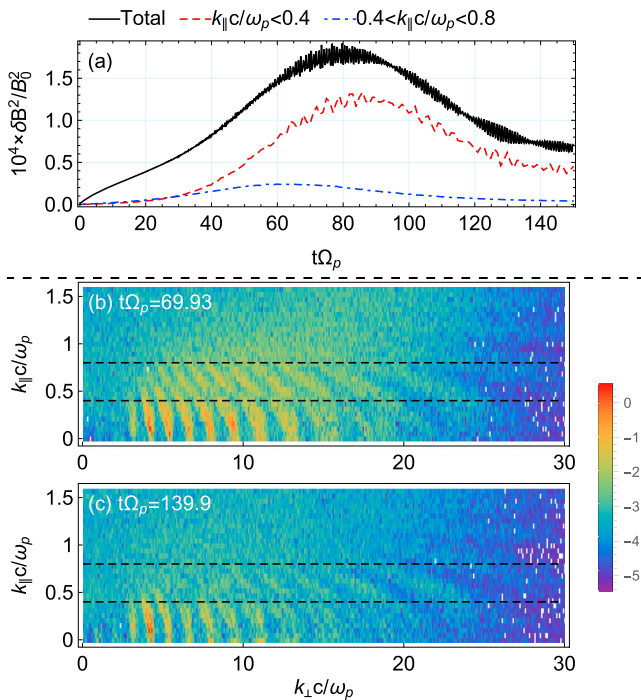
Figure 8. Summary plots of the PIC simulation with $m_p/m_e = 225$. (a) Time evolution of the total fluctuating magnetic field energy density (black solid), the energy density for the full harmonic modes in $|k_\parallel c/\omega_{pp}| \lesssim 0.4$ (red dashed), and the energy density for the half harmonic modes in $0.4 \lesssim |k_\parallel c/\omega_{pp}| \lesssim 0.8$ (blue dash-dotted). (b) Wave number spectrum of the fluctuating magnetic field ($|\delta\mathbf{B}|^2 = |\delta B_x|^2 + |\delta B_y|^2 + |\delta B_z|^2$) at $t\Omega_p \approx 70$. (c) Wave number spectrum of the fluctuating magnetic field at $t\Omega_p \approx 140$. The color scale is in a logarithmic scale, and the white patches in the spectra denote values less than the lower limit.

terminated well beyond the fast magnetosonic wave saturation. No signature of EMIC waves was identified for the duration of simulation runs, likely due to the small pitch angle anisotropy of the partial shell components and the late time development of the EMIC waves (Min et al., 2016). Indeed, the maximum growth rate of the EMIC instability calculated from linear theory is quite small (about $0.006\Omega_p$).

Figure 8 displays the summary of the simulation with $m_p/m_e = 225$. The magnetic field fluctuations saturate at about $t\Omega_p = 80$. The wave number spectrum at this time (Figure 8b) resembles the linear growth pattern in Figure 7b, apart from the number of unstable harmonics. The discrete modes at $|k_\parallel|c/\omega_{pp} \lesssim 0.4$ correspond to the full harmonic modes, whereas the discrete modes at $0.4 \lesssim |k_\parallel|c/\omega_{pp} \lesssim 0.8$ correspond to the half harmonic modes. Above $k_\parallel c/\omega_{pp} \approx 1$ is where the spectrum becomes continuous according to the linear growth rate calculation. Interestingly, the full harmonic modes saturate at a later time and at a much higher level than the half harmonic modes (Figure 8a). Near the end of the simulation (Figure 8c), the half harmonic modes disappeared almost completely, whereas the full harmonic modes still remain. The results of the $m_p/m_e = 100$ run are similar, except for the number of unstable harmonic modes.

Figures 3c and 3d display the frequency power spectra of the magnetic field fluctuations from the simulations with $m_p/m_e = 100$ and 225, respectively. The field fluctuations from many simulation grid points were recorded between $t\Omega_p = 0$ and 150 with a cadence of about $0.1\Omega_p$ for both cases. The individual records at different spatial locations were then Fourier transformed followed by a spatial average. As expected from the wave number spectra in Figures 8b and 8c, the frequency spectra exhibit discrete peaks at the full harmonics with larger amplitude than those of the half harmonics. In both cases, the fourth harmonic has the largest amplitude. The amplitude of the subsequent harmonic modes decreases gradually, while the background level rises slightly. The increase of the background may be in part contributed by the relatively large noise level in the simulations due to the relatively small number of simulation particles. In addition, the half harmonic modes, which have much lower amplitude, are filling the gaps between the full harmonics, as what we suggested might occur for the observations. These half harmonic modes are more clearly visible in the transverse component above the fifth harmonic for $m_p/m_e = 100$ and the ninth harmonic for $m_p/m_e = 225$. The reason for this is that the ratio $|\delta B_\parallel|^2/|\delta B_\perp|^2$ decreases with the decreasing wave normal angle (see, e.g., Boardsen et al., 2016, Figure 1) (also confirmed from the linear theory results).

Similar to the observed spectrum in Figure 3b, the simulations produce a series of discrete peaks at full harmonics. Moreover, the simulations appear to account for the upper frequency bound of the observations well below the lower hybrid frequency. Although the linear Vlasov theory predicts growing modes up to the lower hybrid frequency, the high-frequency modes generally evolve faster and saturate at a lower level than the low-frequency modes. In fact, according to the linear theory results, the fourth harmonic mode indeed has the largest growth rate for $m_p/m_e = 100$, but it is the eighth harmonic mode that has the largest growth rate for $m_p/m_e = 225$. There are a few observational features that the present simulations cannot account for. First, the simulations show the enhancement starting from the third harmonic, which is consistent with the linear theory prediction, but the observations show essentially no wave power below the eighth harmonic except for the fourth harmonic. Second, the slight depression of power near $22\Omega_p$ (about half of the lower hybrid frequency) is not obvious from the simulations. Lastly, there is an order of magnitude difference between the simulated and observed wave amplitudes (not shown). We suspect that this is mainly because the present simulations are for an infinite homogeneous plasma, but in the real magnetosphere, the waves that are excited can leave the source region.

Figures 4b and 4c show the proton differential fluxes captured at the time of wave saturation from the simulations with $m_p/m_e = 100$ and 225, respectively. As expected, the partial shell protons diffuse to lower energy
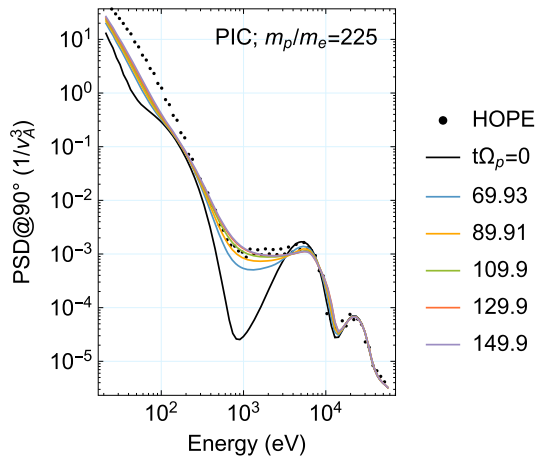
Figure 9. Comparison of the observed and simulated phase space densities at $\alpha = 90°$. The results of the $m_p/m_e = 225$ simulation sampled at $t\Omega_p = 70, 90, 110, 130,$ and 150 are shown with colored curves as labeled. The dots represent the observed phase space density, and the black curve denotes the initial distribution in the simulation.

and the low-energy protons below 1 keV are heated mainly along the perpendicular velocity direction. Consequently, there are small regions near 1 keV and at off-90° pitch angles where the fluxes have not been affected by the waves. In comparison with the observation in Figure 4a, the agreement is quite good above approximately 0.7 keV, including the low flux regions near the loss cone angle. From the color contrast, however, the simulations underestimate (overestimate) the intensity at $\alpha \approx 90°$ ($\alpha \lesssim 45°$) of the low-energy population. As described in subsection 3.1, the discrepancy at small pitch angles can be attributed to imperfect fitting due to the limitation of the bi-Maxwellian distribution.

Figure 9 shows the $\alpha = 90°$ proton phase space density for the $m_p/m_e = 225$ simulation sampled at $t\Omega_p = 70, 90, 110, 130,$ and 150 in comparison with the observed phase space density. By the time of wave saturation ($t\Omega_p \approx 70$), the local minimum at about 1 keV has been already filled up due to the scattering of protons approximately between 0.4 and 5 keV. As a result, the simulated phase space density for $\gtrsim 0.4$ keV is very close to the observed one. As time progresses toward the end of the simulation, the phase space density near 1 keV is enhanced further and the partial shell near 5 keV is slightly reduced. If we continue the simulation without fresh partial shell proton injections, the scattering by the remnant waves will eventually flatten out this partial shell so that the positive slope disappears. The energy diffusion toward high energy also caused the slight enhancement of the phase space density near 10 keV, suggesting that the initial thermal spread of the partial shell may be slightly smaller. In contrast to the high-energy part, the enhancement of the phase space density below 0.3 keV is still far less than the observed level even near the end of the simulation (by a factor of 2 at most). This suggests that the low-energy proton population initially had some degree of pitch angle anisotropy caused by some other mechanisms. Finally, the second peak near 20 keV and the protons at even higher energy exhibit little variation, indicating that they are not affected by the waves.

4. Conclusions and Discussions

Linear Vlasov theory and kinetic simulations for electromagnetic fluctuations in a homogeneous, magnetized, and collisionless plasma were used to investigate a fast magnetosonic wave event observed by the Van Allen Probes. The burst mode waveform data, which were continuously measured for almost 20 min, showed that the fluctuating electric and magnetic fields have a series of spectral peaks at harmonics of the proton cyclotron frequency, Ω_p, between about 8 and $34\Omega_p$ and an isolated peak at the fourth harmonic. Furthermore, the compressional component of the magnetic field fluctuations was much larger (by roughly 2 orders of magnitude) than the transverse component, indicating that the observed waves can be classified as fast magnetosonic waves. The proton phase space density exhibited not one but two local maxima above the Alfvén energy $m_p v_A^2/2$, although it turned out that the waves were primarily driven by the one closer to the Alfvén energy. The harmonic frequency spectrum of the field fluctuations and the positive slopes in the proton phase space density suggested that these waves might have been locally generated.

The subsequent analyses were focused on testing this hypothesis. First, linear dispersion analyses were performed. Initially, four bi-Maxwellian distributions and two partial shell distributions were used to represent the observed proton phase space density, which we labeled Model 1. For electrons, a single bi-Maxwellian with a low temperature was used to represent the whole electron population because the warmer electrons measured only constituted about 1% of the total. The linear theory predicted relatively small growth rates at full harmonics and relatively large growth rates at half harmonics. Because this is at variance with the observed harmonic pattern, we hypothesized that the observed proton distribution is already in a marginally stable state after the wave excitation. Since interactions with fast magnetosonic waves primarily lead to perpendicular scattering of the proton velocity distribution, Model 1 was modified to roll back the effects of this characteristic scattering. Consequently, the modified proton distribution, Model 2, is more unstable than Model 1, and the full harmonic modes are more unstable than the half harmonic modes.

PIC simulations were then initialized with Model 2 to examine the excitation of fast magnetosonic waves and the evolution of the proton distribution. Due to the limited computational resources, smaller values for the

proton-to-electron mass ratio m_p/m_e had to be used; for the present study two simulations were performed with $m_p/m_e = 100$ and 225, respectively. The results from the two simulations were qualitatively consistent with each other. The self-consistently evolved proton distribution is in general quite consistent with the observations. Interactions with the excited fast magnetosonic waves resulted in the preferential perpendicular velocity scattering of energetic partial shell protons as well as low-energy protons. Consequently, the positive slope, which is the source of free energy, was greatly reduced toward the observed level. The heating of lower-energy ($\lesssim 0.3$ keV) protons in the simulations was less substantial than the observation, suggesting that this population was initially anisotropic. The excited fast magnetosonic waves in the simulations exhibited a series of spectral peaks at full harmonics, consistent with the observations. Although linear theory predicts substantial growth of half harmonic modes, the nonlinear evolution allowed the full harmonic modes at propagation quasi-perpendicular to $\mathbf{B}_0$ to grow stronger and persist longer. The good agreement between the observed and simulated proton distributions is evidence for resonant interactions taking place between the energetic protons and the observed fast magnetosonic waves that may have been generated locally. The fact that the observed proton distribution corresponds to a marginally stable state when the distribution has already been scattered by the excited waves indicates that linear theory alone may not be sufficient to interpret fast magnetosonic wave observations.

While the agreement between the observed and simulated proton distributions can be improved by fine-tuning the initial distribution, there are some features in the observed wave spectrum that the present analyses do not seem to account for: the lower frequency bound of the spectrum with an isolated fourth harmonic and the slight depression of wave power at an intermediate frequency. We explored the effect of suprathermal electrons that were not included in the simulations due to their low concentration. We found that they can lead to a slight reduction of growth rates preferentially at propagation away from perpendicular directions but cannot account for the aforementioned features (see the supporting information). We also examined the effect of a smaller multiplication factor used to adjust the HOPE proton measurement (as suggested by Kistler et al., 2016), but it could not account for those features. As for the lower frequency bound, a possible explanation in the realm of a homogeneous, infinite plasma is uncertainties in the measurement and/or the model distribution fitting. Boardsen et al. (1992), Horne et al. (2000), and Chen et al. (2010) showed that the lower frequency bound of the fast magnetosonic waves is determined by the ratio of the ring/shell speed to the Alfvén speed. A simple estimate of growth rates at perpendicular propagation (equation (A41) of Min & Liu, 2016a) suggests that the uncertainty in the measurement and/or the model distribution fitting by three or four energy bins could resolve the mismatch of the lower frequency bound between the linear theory prediction and the observations. However, this uncertainty still cannot explain the isolated fourth harmonic peak. With several options exhausted in the realm of a homogeneous, infinite plasma, inclusion of propagation in a nonuniform magnetic field may be necessary to explain the details of the observed wave spectrum, especially the fourth harmonic. A good description of these waves may require the inclusion of the dipole magnetic field geometry as has been done, for example, by Hu and Denton (2009) for the excitation and propagation of EMIC waves.

Appendix A: Approximation of Partial Shell Distribution for Linear Dispersion Analysis

The partial shell distribution of equation (1) can be written as

$$F_s(x, \alpha) = \frac{1}{\pi^{3/2} C(x_s)} e^{-(x-x_s)^2} \sin^\sigma \alpha, \tag{A1}$$

where x_s is the shell speed normalized to the thermal spread. Following Min and Liu (2015a), F_s can be approximately represented by

$$F_s \approx \sum_{j=-1}^{N+1} \eta_j F_r(x_{d,j}, x_{r,j}; x_\parallel, x_\perp), \tag{A2}$$

where

$$F_r(x_d, x_r; x_\parallel, x_\perp) = \frac{1}{\pi^{3/2} A(x_r)} e^{-(x_\parallel - x_d)^2} e^{-(x_\perp - x_r)^2} \tag{A3}$$

is a ring beam distribution with a normalization constant $A(x) = e^{-x^2} + \sqrt{\pi}x \, \text{erfc}(-x)$. The parameters in equation (A2) are determined as follows: $x_{d,j} = x'_s \cos(\pi j/N)$, $x_{r,j} = x'_s \sin(\pi j/N)$, and $\eta_j = \sin^\sigma(\pi j/N) A(x_{r,j}) / \sum_{l=-1}^{N+1} \sin^\sigma(\pi l/N) A(x_{r,l})$. The unknowns, N and x'_s, are determined by trial and error to minimize the difference between the exact and approximate shells. For the present study, we find that choosing $x'_s = 4.01$ and $N = 11$ for the partial shell component 5, and $x'_s = 5.96$ and $N = 16$ for the partial shell component 6 in Table 1 results in an approximate shell sufficiently close to the exact one.

References

Albert, J. M., Starks, M. J., Horne, R. B., Meredith, N. P., & Glauert, S. A. (2016). Quasi-linear simulations of inner radiation belt electron pitch angle and energy distributions. *Geophysical Research Letters*, *43*, 2381–2388. https://doi.org/10.1002/2016GL067938

Artemyev, A. V., Mourenas, D., Agapitov, O. V., & Krasnoselskikh, V. V. (2015). Relativistic electron scattering by magnetosonic waves: Effects of discrete wave emission and high wave amplitudes. *Physics of Plasmas*, *22*(6), 062901. https://doi.org/10.1063/1.4922061

Ashour-Abdalla, M., Leboeuf, J. N., Schriver, D., Bosqued, J.-M., Cornilleau-Wehrlin, N., Sotnikov, V., . . . Fazakerley, A. N. (2006). Instabilities driven by ion shell distributions observed by Cluster in the midaltitude plasma sheet boundary layer. *Journal of Geophysical Research*, *111*, A10223. https://doi.org/10.1029/2005JA011490

Balikhin, M. A., Shprits, Y. Y., Walker, S. N., Chen, L., Cornilleau-Wehrlin, N., Dandouras, I., . . . Weiss, B. (2015). Observations of discrete harmonics emerging from equatorial noise. *Nature Communications*, *6*, 7703. https://doi.org/10.1038/ncomms8703

Boardsen, S. A., Gallagher, D. L., Gurnett, D. A., Peterson, W. K., & Green, J. L. (1992). Funnel-shaped, low-frequency equatorial waves. *Journal of Geophysical Research*, *97*, 14. https://doi.org/10.1029/92JA00827

Boardsen, S. A., Hospodarsky, G. B., Kletzing, C. A., Engebretson, M. J., Pfaff, R. F., Wygant, J. R., . . . De Pascuale, S. (2016). Survey of the frequency dependent latitudinal distribution of the fast magnetosonic wave mode from Van Allen Probes Electric and Magnetic Field Instrument and Integrated Science waveform receiver plasma wave analysis. *Journal of Geophysical Research: Space Physics*, *121*, 2902–2921. https://doi.org/10.1002/2015JA021844

Boardsen, S. A., Hospodarsky, G. B., Kletzing, C. A., Pfaff, R. F., Kurth, W. S., Wygant, J. R., & MacDonald, E. A. (2014). Van Allen Probe observations of periodic rising frequencies of the fast magnetosonic mode. *Geophysical Research Letters*, *41*, 8161–8168. https://doi.org/10.1002/2014GL062020

Bortnik, J., Thorne, R. M., Ni, B., & Li, J. (2015). Analytical approximation of transit time scattering due to magnetosonic waves. *Geophysical Research Letters*, *42*, 1318–1325. https://doi.org/10.1002/2014GL062710

Chen, L. (2015). Wave normal angle and frequency characteristics of magnetosonic wave linear instability. *Geophysical Research Letters*, *42*, 4709–4715. https://doi.org/10.1002/2015GL064237

Chen, L., Maldonado, A., Bortnik, J., Thorne, R. M., Li, J., Dai, L., & Zhan, X. (2015). Nonlinear bounce resonances between magnetosonic waves and equatorially mirroring electrons. *Journal of Geophysical Research: Space Physics*, *120*, 6514–6527. https://doi.org/10.1002/2015JA021174

Chen, L., Sun, J., Lu, Q., Gao, X., Xia, Z., & Zhima, Z. (2016). Generation of magnetosonic waves over a continuous spectrum. *Journal of Geophysical Research: Space Physics*, *121*, 1137–1147. https://doi.org/10.1002/2015JA022089

Chen, L., Thorne, R. M., Jordanova, V. K., & Horne, R. B. (2010). Global simulation of magnetosonic wave instability in the storm time magnetosphere. *Journal of Geophysical Research: Space Physics*, *115*, A11222. https://doi.org/10.1029/2010JA015707

Coroniti, F. V., Fredricks, R. W., & White, R. (1972). Instability of ring current protons beyond the plasmapause during injection events. *Journal of Geophysical Research*, *77*, 6243–6248. https://doi.org/10.1029/JA077i031p06243

Curtis, S. A., & Wu, C. S. (1979). Gyroharmonic emissions induced by energetic ions in the equatorial plasmasphere. *Journal of Geophysical Research*, *84*, 2597–2607. https://doi.org/10.1029/JA084iA06p02597

Davidson, R. C., & Ogden, J. M. (1975). Electromagnetic ion cyclotron instability driven by ion energy anisotropy in high-beta plasmas. *Physics of Fluids*, *18*, 1045–1050. https://doi.org/10.1063/1.861253

Denton, R. E., Engebretson, M. J., Keiling, A., Walsh, A. P., Gary, S. P., DéCréAu, P. M. E., . . . RèMe, H. (2010). Multiple harmonic ULF waves in the plasma sheet boundary layer: Instability analysis. *Journal of Geophysical Research*, *115*, A12224. https://doi.org/10.1029/2010JA015928

Denton, R. E., Hudson, M. K., Fuselier, S. A., & Anderson, B. J. (1993). Electromagnetic ion cyclotron waves in the plasma depletion layer. *Journal of Geophysical Research*, *98*, 13,477–13,490. https://doi.org/10.1029/93JA00796

Freund, H. P., & Wu, C. S. (1988). Stability of a spherical shell distribution of pickup ions. *Journal of Geophysical Research*, *93*, 14,277–14,283. https://doi.org/10.1029/JA093iA12p14277

Fu, H. S., Cao, J. B., Zhima, Z., Khotyaintsev, Y. V., Angelopoulos, V., Santolík, O., . . . Huang, S. Y. (2014). First observation of rising-tone magnetosonic waves. *Geophysical Research Letters*, *41*, 7419–7426. https://doi.org/10.1002/2014GL061867

Fu, X., Cowee, M. M., Friedel, R. H., Funsten, H. O., Gary, S. P., Hospodarsky, G. B., . . . Winske, D. (2014). Whistler anisotropy instabilities as the source of banded chorus: Van Allen Probes observations and particle-in-cell simulations. *Journal of Geophysical Research: Space Physics*, *119*, 8288–8298. https://doi.org/10.1002/2014JA020364

Funsten, H. O., Skoug, R. M., Guthrie, A. A., MacDonald, E. A., Baldonado, J. R., Harper, R. W., . . . Chen, J. (2013). Helium, Oxygen, Proton, and Electron (HOPE) Mass Spectrometer for the Radiation Belt Storm Probes mission. *Space Science Reviews*, *179*, 423–484. https://doi.org/10.1007/s11214-013-9968-7

Gao, X., Liu, K., Wang, X., Min, K., Lin, Y., & Wang, X. (2017). Gyrokinetic electron and fully kinetic ion simulations of fast magnetosonic waves in the magnetosphere. *Physics of Plasmas*, *24*(6), 062901. https://doi.org/10.1063/1.4985303

Gary, S. P., Liu, K., & Winske, D. (2011). Bernstein instability driven by suprathermal protons in the ring current. *Journal of Geophysical Research*, *116*, A08215. https://doi.org/10.1029/2011JA016543

Gary, S. P., Liu, K., Winske, D., & Denton, R. E. (2010). Ion Bernstein instability in the terrestrial magnetosphere: Linear dispersion theory. *Journal of Geophysical Research*, *115*, A12209. https://doi.org/10.1029/2010JA015965

Gulelmi, A. V., Klaine, B. I., & Potapov, A. S. (1975). Excitation of magnetosonic waves with discrete spectrum in the equatorial vicinity of the plasmapause. *Planetary and Space Science*, *23*, 279–286. https://doi.org/10.1016/0032-0633(75)90133-6

Gurnett, D. A. (1976). Plasma wave interactions with energetic ions near the magnetic equator. *Journal of Geophysical Research*, *81*, 2765–2770. https://doi.org/10.1029/JA081i016p02765

Horne, R. B., Thorne, R. M., Glauert, S. A., Meredith, N. P., Pokhotelov, D., & Santolík, O. (2007). Electron acceleration in the Van Allen radiation belts by fast magnetosonic waves. *Geophysical Research Letters*, *34*, L17107. https://doi.org/10.1029/2007GL030267

Horne, R. B., Wheeler, G. V., & Alleyne, H. S. C. K. (2000). Proton and electron heating by radially propagating fast magnetosonic waves. *Journal of Geophysical Research*, *105*, 27,597–27,610. https://doi.org/10.1029/2000JA000018

Hrbáčková, Z., Santolík, O., Němec, F., Macúšová, E., & Cornilleau-Wehrlin, N. (2015). Systematic analysis of occurrence of equatorial noise emissions using 10 years of data from the Cluster mission. *Journal of Geophysical Research: Space Physics*, *120*, 1007–1021. https://doi.org/10.1002/2014JA020268

Hu, Y., & Denton, R. E. (2009). Two-dimensional hybrid code simulation of electromagnetic ion cyclotron waves in a dipole magnetic field. *Journal of Geophysical Research*, *114*, A12217. https://doi.org/10.1029/2009JA014570

Janhunen, P., Olsson, A., Vaivads, A., & Peterson, W. K. (2003). Generation of Bernstein waves by ion shell distributions in the auroral region. *Annales Geophysicae*, *21*, 881–891. https://doi.org/10.5194/angeo-21-881-2003

Jordanova, V. K., Welling, D. T., Zaharia, S. G., Chen, L., & Thorne, R. M. (2012). Modeling ring current ion and electron dynamics and plasma instabilities during a high-speed stream driven storm. *Journal of Geophysical Research*, *117*, A00L08. https://doi.org/10.1029/2011JA017433

Kistler, L. M., Mouikis, C. G., Spence, H. E., Menz, A. M., Skoug, R. M., Funsten, H. O., … Lanzerotti, L. J. (2016). The source of O^+ in the storm time ring current. *Journal of Geophysical Research: Space Physics*, *121*, 5333–5349. https://doi.org/10.1002/2015JA022204

Kletzing, C. A., Kurth, W. S., Acuna, M., MacDowall, R. J., Torbert, R. B., Averkamp, T., … Tyler, J. (2013). The Electric and Magnetic Field Instrument Suite and Integrated Science (EMFISIS) on RBSP. *Space Science Reviews*, *179*, 127–181. https://doi.org/10.1007/s11214-013-9993-6

Laakso, H., Junginger, H., Schmidt, R., Roux, A., & de Villedary, C. (1990). Magnetosonic waves above $f_c(H^+)$ at geostationary orbit—GEOS 2 results. *Journal of Geophysical Research*, *95*, 10,609–10,621. https://doi.org/10.1029/JA095iA07p10609

Li, J., Bortnik, J., Li, W., Ma, Q., Thorne, R. M., Kletzing, C. A., … Russell, C. T. (2017). "Zipper-like" periodic magnetosonic waves: Van Allen Probes, THEMIS, and Magnetospheric Multiscale observations. *Journal of Geophysical Research: Space Physics*, *122*, 1600–1610. https://doi.org/10.1002/2016JA023536

Li, J., Bortnik, J., Thorne, R. M., Li, W., Ma, Q., Baker, D. N., … Blake, J. B. (2016). Ultrarelativistic electron butterfly distributions created by parallel acceleration due to magnetosonic waves. *Journal of Geophysical Research: Space Physics*, *121*, 3212–3222. https://doi.org/10.1002/2016JA022370

Li, J., Ni, B., Xie, L., Pu, Z., Bortnik, J., Thorne, R. M., … Guo, R. (2014). Interactions between magnetosonic waves and radiation belt electrons: Comparisons of quasi-linear calculations with test particle simulations. *Geophysical Research Letters*, *41*, 4828–4834. https://doi.org/10.1002/2014GL060461

Li, X., Tao, X., Lu, Q., & Dai, L. (2015). Bounce resonance diffusion coefficients for spatially confined waves. *Geophysical Research Letters*, *42*, 9591–9599. https://doi.org/10.1002/2015GL066324

Lin, Y., Wang, X. Y., Chen, L., Lu, X., & Kong, W. (2011). An improved gyrokinetic electron and fully kinetic ion particle simulation scheme: Benchmark with a linear tearing mode. *Plasma Physics and Controlled Fusion*, *53*(5), 054013. https://doi.org/10.1088/0741-3335/53/5/054013

Lin, Y., Wang, X., Lin, Z., & Chen, L. (2005). A gyrokinetic electron and fully kinetic ion plasma simulation model. *Plasma Physics and Controlled Fusion*, *47*, 657–669. https://doi.org/10.1088/0741-3335/47/4/006

Liu, K. (2007). *Particle-in-cell simulations of particle energization in the auroral region*. New York: Cornell University.

Liu, K., Gary, S. P., & Winske, D. (2011). Excitation of magnetosonic waves in the terrestrial magnetosphere: Particle-in-cell simulations. *Journal of Geophysical Research*, *116*, A07212. https://doi.org/10.1029/2010JA016372

Ma, Q., Li, W., Chen, L., Thorne, R. M., & Angelopoulos, V. (2014). Magnetosonic wave excitation by ion ring distributions in the Earth's inner magnetosphere. *Journal of Geophysical Research: Space Physics*, *119*, 844–852. https://doi.org/10.1002/2013JA019591

Ma, Q., Li, W., Chen, L., Thorne, R. M., Kletzing, C. A., Kurth, W. S., … Spence, H. E. (2014). The trapping of equatorial magnetosonic waves in the Earth's outer plasmasphere. *Geophysical Research Letters*, *41*, 6307–6313. https://doi.org/10.1002/2014GL061414

Ma, Q., Li, W., Thorne, R. M., & Angelopoulos, V. (2013). Global distribution of equatorial magnetosonic waves observed by THEMIS. *Geophysical Research Letters*, *40*, 1895–1901. https://doi.org/10.1002/grl.50434

Ma, Q., Li, W., Thorne, R. M., Bortnik, J., Kletzing, C. A., Kurth, W. S., & Hospodarsky, G. B. (2016). Electron scattering by magnetosonic waves in the inner magnetosphere. *Journal of Geophysical Research: Space Physics*, *121*, 274–285. https://doi.org/10.1002/2015JA021992

Maldonado, A. A., Chen, L., Claudepierre, S. G., Bortnik, J., Thorne, R. M., & Spence, H. (2016). Electron butterfly distribution modulation by magnetosonic waves. *Geophysical Research Letters*, *43*, 3051–3059. https://doi.org/10.1002/2016GL068161

Mauk, B. H., Fox, N. J., Kanekal, S. G., Kessel, R. L., Sibeck, D. G., & Ukhorskiy, A. (2013). Science objectives and rationale for the Radiation Belt Storm Probes mission. *Space Science Reviews*, *179*, 3–27. https://doi.org/10.1007/s11214-012-9908-y

McClements, K. G., Dendy, R. O., & Lashmore-Davis, C. N. (1994). A model for the generation of obliquely propagating ULF waves near the magnetic equator. *Journal of Geophysical Research*, *99*, 23,685–23,693. https://doi.org/10.1029/94JA01979

Meredith, N. P., Horne, R. B., & Anderson, R. R. (2008). Survey of magnetosonic waves and proton ring distributions in the Earth's inner magnetosphere. *Journal of Geophysical Research*, *113*, A06213. https://doi.org/10.1029/2007JA012975

Min, K., & Liu, K. (2015a). Fast magnetosonic waves driven by shell velocity distributions. *Journal of Geophysical Research: Space Physics*, *120*, 2739–2753. https://doi.org/10.1002/2015JA021041

Min, K., & Liu, K. (2015b). Regime transition of ion Bernstein instability driven by ion shell velocity distributions. *Journal of Geophysical Research: Space Physics*, *120*, 8448–8454. https://doi.org/10.1002/2015JA021514

Min, K., & Liu, K. (2016a). Ion Bernstein instability dependence on the proton-to-electron mass ratio: Linear dispersion theory. *Journal of Geophysical Research: Space Physics*, *121*, 6692–6710. https://doi.org/10.1002/2016JA022850

Min, K., & Liu, K. (2016b). Proton velocity ring-driven instabilities in the inner magnetosphere: Linear theory and particle-in-cell simulations. *Journal of Geophysical Research: Space Physics*, *121*, 475–491. https://doi.org/10.1002/2015JA022042

Min, K., & Liu, K. (2016c). Understanding the growth rate patterns of ion Bernstein instabilities driven by ring-like proton velocity distributions. *Journal of Geophysical Research: Space Physics*, *121*, 3036–3049. https://doi.org/10.1002/2016JA022524

Min, K., Liu, K., & Gary, S. P. (2016). Scalings of Alfvén-cyclotron and ion Bernstein instabilities on temperature anisotropy of a ring-like velocity distribution in the inner magnetosphere. *Journal of Geophysical Research: Space Physics*, *121*, 2185–2193. https://doi.org/10.1002/2015JA022134

Min, K., Takahashi, K., Ukhorskiy, A. Y., Manweiler, J. W., Spence, H. E., Singer, H., … Cohen, R. J. (2017). Second harmonic poloidal waves observed by Van Allen Probes in the dusk-midnight sector. *Journal of Geophysical Research: Space Physics*, *122*, 3013–3039. https://doi.org/10.1002/2016JA023770

Mitchell, D. G., Lanzerotti, L. J., Kim, C. K., Stokes, M., Ho, G., Cooper, S., … Kerem, S. (2013). Radiation Belt Storm Probes Ion Composition Experiment (RBSPICE). *Space Science Reviews*, *179*, 263–308. https://doi.org/10.1007/s11214-013-9965-x

Mourenas, D., Artemyev, A. V., Agapitov, O. V., & Krasnoselskikh, V. (2013). Analytical estimates of electron quasi-linear diffusion by fast magnetosonic waves. *Journal of Geophysical Research: Space Physics*, *118*, 3096–3112. https://doi.org/10.1002/jgra.50349

Ni, B., Hua, M., Zhou, R., Yi, J., & Fu, S. (2017). Competition between outer zone electron scattering by plasmaspheric hiss and magnetosonic waves. *Geophysical Research Letters*, *44*, 3465–3474. https://doi.org/10.1002/2017GL072989

Němec, F., Santolík, O., Hrbáčková, Z., & Cornilleau-Wehrlin, N. (2015). Intensities and spatiotemporal variability of equatorial noise emissions observed by the Cluster spacecraft. *Journal of Geophysical Research: Space Physics*, *120*, 1620–1632. https://doi.org/10.1002/2014JA020814

Němec, F., Santolík, O., Gereová, K., Macúšová, E., de Conchy, Y., & Cornilleau-Wehrlin, N. (2005). Initial results of a survey of equatorial noise emissions observed by the Cluster spacecraft. *Planetary and Space Science*, *53*, 291–298. https://doi.org/10.1016/j.pss.2004.09.055

Němec, F., Santolík, O., Gereová, K., Macúšová, E., Laakso, H., de Conchy, Y., . . . Cornilleau-Wehrlin, N. (2006). Equatorial noise: Statistical study of its localization and the derived number density. *Advances in Space Research*, *37*, 610–616. https://doi.org/10.1016/j.asr.2005.03.025

Němec, F., Santolík, O., Hrbáčková, Z., Pickett, J. S., & Cornilleau-Wehrlin, N. (2015). Equatorial noise emissions with quasiperiodic modulation of wave intensity. *Journal of Geophysical Research: Space Physics*, *120*, 2649–2661. https://doi.org/10.1002/2014JA020816

Perraut, S., Roux, A., Robert, P., Gendrin, R., Sauvaud, J.-A., Bosqued, J.-M., . . . Korth, A. (1982). A systematic study of ULF waves above F/H plus/ from GEOS 1 and 2 measurements and their relationships with proton ring distributions. *Journal of Geophysical Research*, *87*, 6219–6236. https://doi.org/10.1029/JA087iA08p06219

Posch, J. L., Engebretson, M. J., Olson, C. N., Thaller, S. A., Breneman, A. W., Wygant, J. R., . . . Reeves, G. D. (2015). Low-harmonic magnetosonic waves observed by the Van Allen Probes. *Journal of Geophysical Research: Space Physics*, *120*, 6230–6257. https://doi.org/10.1002/2015JA021179

Russell, C. T., Holzer, R. E., & Smith, E. J. (1970). OGO 3 observations of ELF noise in the magnetosphere: 2. The nature of the equatorial noise. *Journal of Geophysical Research*, *75*, 755–768. https://doi.org/10.1029/JA075i004p00755

Santolík, O., Gurnett, D., & Pickett, J. (2004). Multipoint investigation of the source region of storm-time chorus. *Annales Geophysicae*, *22*, 2555–2563. https://doi.org/10.5194/angeo-22-2555-2004

Santolík, O., Parrot, M., & Němec, F. (2016). Propagation of equatorial noise to low altitudes: Decoupling from the magnetosonic mode. *Geophysical Research Letters*, *43*, 6694–6704. https://doi.org/10.1002/2016GL069582

Santolík, O., Pickett, J. S., Gurnett, D. A., Maksimovic, M., & Cornilleau-Wehrlin, N. (2002). Spatiotemporal variability and propagation of equatorial noise observed by Cluster. *Journal of Geophysical Research*, *107*(A12), 1495. https://doi.org/10.1029/2001JA009159

Shprits, Y. Y. (2016). Estimation of bounce resonant scattering by fast magnetosonic waves. *Geophysical Research Letters*, *43*, 998–1006. https://doi.org/10.1002/2015GL066796

Shprits, Y. Y., Runov, A., & Ni, B. (2013). Gyro-resonant scattering of radiation belt electrons during the solar minimum by fast magnetosonic waves. *Journal of Geophysical Research: Space Physics*, *118*, 648–652. https://doi.org/10.1002/jgra.50108

Spence, H. E., Reeves, G. D., Baker, D. N., Blake, J. B., Bolton, M., Bourdarie, S., . . . Thorne, R. M. (2013). Science goals and overview of the Radiation Belt Storm Probes (RBSP) Energetic Particle, Composition, and Thermal Plasma (ECT) suite on NASA's Van Allen Probes mission. *Space Science Reviews*, *179*, 311–336. https://doi.org/10.1007/s11214-013-0007-5

Su, Z., Wang, G., Liu, N., Zheng, H., Wang, Y., & Wang, S. (2017). Direct observation of generation and propagation of magnetosonic waves following substorm injection. *Geophysical Research Letters*, *44*, 7587–7597. https://doi.org/10.1002/2017GL074362

Sun, J., Gao, X., Lu, Q., Chen, L., Tao, X., & Wang, S. (2016). A parametric study for the generation of ion Bernstein modes from a discrete spectrum to a continuous one in the inner magnetosphere. II. Particle-in-cell simulations. *Physics of Plasmas*, *23*(2), 022902. https://doi.org/10.1063/1.4941284

Sun, J., Gao, X., Lu, Q., Chen, L., Liu, X., Wang, X., . . . Wang, S. (2017). Spectral properties and associated plasma energization by magnetosonic waves in the Earth's magnetosphere: Particle-in-cell simulations. *Journal of Geophysical Research: Space Physics*, *122*, 5377–5390. https://doi.org/10.1002/2017JA024027

Tao, X., Chen, L., Liu, X., Lu, Q., & Wang, S. (2017). Quasilinear analysis of saturation properties of broadband whistler mode waves. *Geophysical Research Letters*, *44*, 8122–8129. https://doi.org/10.1002/2017GL074881

Tao, X., & Li, X. (2016). Theoretical bounce resonance diffusion coefficient for waves generated near the equatorial plane. *Geophysical Research Letters*, *43*, 7389–7397. https://doi.org/10.1002/2016GL070139

Thomsen, M. F., Denton, M. H., Gary, S. P., Liu, K., & Min, K. (2017). Ring/Shell ion distributions at geosynchronous orbit. *Journal of Geophysical Research: Space Physics*, *122*, 12,055–12,071. https://doi.org/10.1002/2017JA024612

Thomsen, M. F., Denton, M. H., Jordanova, V. K., Chen, L., & Thorne, R. M. (2011). Free energy to drive equatorial magnetosonic wave instability at geosynchronous orbit. *Journal of Geophysical Research*, *116*, A08220. https://doi.org/10.1029/2011JA016644

Tsurutani, B. T., Falkowski, B. J., Pickett, J. S., Verkhoglyadova, O. P., Santolik, O., & Lakhina, G. S. (2014). Extremely intense ELF magnetosonic waves: A survey of polar observations. *Journal of Geophysical Research: Space Physics*, *119*, 964–977. https://doi.org/10.1002/2013JA019284

Walker, S. N., Balikhin, M. A., Shklyar, D. R., Yearby, K. H., Canu, P., Carr, C. M., & Dandouras, I. (2015). Experimental determination of the dispersion relation of magnetosonic waves. *Journal of Geophysical Research: Space Physics*, *120*, 9632–9650. https://doi.org/10.1002/2015JA021746

Walker, S. N., Demekhov, A. G., Boardsen, S. A., Ganushkina, N. Y., Sibeck, D. G., & Balikhin, M. A. (2016). Cluster observations of non-time continuous magnetosonic waves. *Journal of Geophysical Research: Space Physics*, *121*, 9701–9716. https://doi.org/10.1002/2016JA023287

Walker, S. N., & Moiseenko, I. (2013). Determination of wave vectors using the phase differencing method. *Annales Geophysicae*, *31*, 1611–1617. https://doi.org/10.5194/angeo-31-1611-2013

Xiao, F., Yang, C., Su, Z., Zhou, Q., He, Z., He, Y., . . . Blake, J. B. (2015). Wave-driven butterfly distribution of Van Allen belt relativistic electrons. *Nature Communications*, *6*, 8590. https://doi.org/10.1038/ncomms9590

Xiao, F., Zhou, Q., He, Z., & Tang, L. (2012). Three-dimensional ray tracing of fast magnetosonic waves. *Journal of Geophysical Research*, *117*, A06208. https://doi.org/10.1029/2012JA017589

Xiao, F., Zhou, Q., He, Z., Yang, C., He, Y., & Tang, L. (2013). Magnetosonic wave instability by proton ring distributions: Simultaneous data and modeling. *Journal of Geophysical Research: Space Physics*, *118*, 4053–4058. https://doi.org/10.1002/jgra.50401

Xiao, F., Zhou, Q., He, Y., Yang, C., Liu, S., Baker, D. N., . . . Blake, J. B. (2015). Penetration of magnetosonic waves into the plasmasphere observed by the Van Allen Probes. *Geophysical Research Letters*, *42*, 7287–7294. https://doi.org/10.1002/2015GL065745

Yang, C., Zhang, L., He, Y., Liu, S., & Zhou, Q. (2014). Radiation belt electron acceleration induced by gyroresonant interaction with magnetosonic waves. *Astrophysics and Space Science*, *353*, 389–394. https://doi.org/10.1007/s10509-014-2046-0

Zhima, Z., Chen, L., Fu, H., Cao, J., Horne, R. B., & Reeves, G. (2015). Observations of discrete magnetosonic waves off the magnetic equator. *Geophysical Research Letters*, *42*, 9694–9701. https://doi.org/10.1002/2015GL066255

Zhou, Q., Xiao, F., Yang, C., Liu, S., Kletzing, C. A., Kurth, W. S., . . . Wygant, J. R. (2014). Excitation of nightside magnetosonic waves observed by Van Allen Probes. *Journal of Geophysical Research: Space Physics*, *119*, 9125–9133. https://doi.org/10.1002/2014JA020481